



Dynamic weakening with grain-damage and implications for slab detachment



Ashley Bellas^{a,*}, Shijie Zhong^a, David Bercovici^b, Elvira Mulyukova^b

^a Department of Physics, University of Colorado at Boulder, Boulder, CO 80309-0390, USA

^b Department of Geology and Geophysics, Yale University, New Haven, CT 06520 8109, USA

1. Introduction

The Earth's mantle is currently in a state of active convection such that mantle flow is accompanied by continual overturn of the upper thermal boundary layer or lithosphere. It is widely recognized that subduction of cold, dense oceanic lithosphere supplies the dominant driving force of plate motion and mantle convection (Hager and O'Connell, 1981). However, heavy slabs can detach from the overlying plate, possibly by either a necking instability, plastic-brittle failure, or plastic yielding (Schmalholz, 2011; Duretz et al., 2012; Andrews and Billen, 2007). Detached slabs are observed in the upper mantle as pinched tomographic features (Wortel and Spakman, 2000; Fukao et al., 2001), and could potentially explain precipitous changes in plate motion (Richards and Lithgow-Bertelloni, 1996). Tectonic events which occur on timescales shorter than 10–100 Myrs (a typical transit time across the mantle) are not readily explained by reorientation of mantle flow. It has been proposed that subduction of thickened crust, such as an oceanic plateau or a mid-ocean ridge system, could trigger cessation of subduction and lead to detachment of the downgoing slab (von Blanckenburg and Davies, 1995; Bercovici et al., 2015). Detachment may be responsible for observations of abrupt tectonic events if detachment itself is a rapid process. For example, it is possible that the collision of the Ontong-Java Plateau with the Melanesian arc hindered further subduction of the Pacific plate and caused a rotation of the Pacific plate at 6 Ma (Austermann et al., 2011). Another possible example is that at 50 Ma, a slab imposing a northward driving force on the Pacific plate detached, and reorganized plate motion to produce the bend in the Emperor-Hawaiian seamounts (Bercovici et al., 2015).

For the detachment of a downgoing slab to be a rapid process relative to mantle convection, dynamic weakening on short timescales is required. In this study, we explore the dynamics of a subducted slab using damage theory, which may provide a mechanism for abrupt tectonics (Bercovici et al., 2015). We develop a model based on mantle rheology with diffusion and dislocation creep including grainsize evolution, following Foley et al. (2012), Ricard and Bercovici (2009), and Bercovici et al. (2015). The implemented rheology simulates high-temperature creep in monomineralic and polymimetic grain

assemblages and is consistent with field and laboratory observations (Montési and Hirth, 2003). We explore the coupling of grainsize-, temperature- and stress-dependent viscosity, and grainsize evolution from damage and its effect on slab detachment, while ignoring other potentially relevant features such as composition, 3D geometry, melting, hydration, phase changes, deformation by plastic yielding and shear heating (Gerya et al., 2004; Andrews and Billen, 2007; Billen, 2008; Stegman et al., 2010). Our study aims to address the following questions. How are grainsize evolution and slab detachment coupled? Under which conditions do a necking instability and slab detachment occur, and on what timescale? How is the existence and value of a minimum grainsize controlled by the damage?

This paper is organized as follows: the methods and models are presented in Section 2, and the results in Section 3. Our results focus on three topics: 1) a comparison of the evolution of the slab, focusing on viscosity, stress, and grainsize in convection calculations, 2) the characteristic timescale on which a necking instability develops, and 3) a slab decoupling timescale. Discussion and conclusions follow in Sections 4 and 5, respectively.

2. Methods and models

In this section, we present the model, governing equations and rheological equations coupled with grainsize evolution. We discuss solution methods, particularly, a new iterative scheme for non-linear viscosity and a particle-based method for solving the grainsize evolution equation.

2.1. Governing equations

Convection calculations are formulated for time-dependent, dynamically self-consistent thermal convection in 2-D Cartesian geometry. The mantle is treated as an incompressible fluid with constant thermodynamic properties and we exclude internal heat production. The dimensionless conservation equations of mass, momentum, and energy for mantle convection in the Boussinesq approximation and infinite Prandtl number limit are

* Corresponding author.

E-mail address: ashley.bellas@colorado.edu (A. Bellas).

$$\nabla \cdot \mathbf{u} = 0 \quad (1)$$

$$-\nabla P + \nabla \cdot [\eta(\nabla \mathbf{u} + \nabla^T \mathbf{u})] + Ra\Theta \hat{\mathbf{e}}_z = 0, \quad (2)$$

$$\frac{\partial \Theta}{\partial t} + \mathbf{u} \cdot \nabla \Theta = \nabla^2 \Theta, \quad (3)$$

following Schubert, Turcotte and Olson (2001), where \mathbf{u} is the velocity vector, P the pressure, η the viscosity, $\hat{\mathbf{e}}_z$ the unit vector in the vertical direction, Θ the temperature, and Ra is the Rayleigh number. The non-dimensionalization of the governing equations is given in Appendix A.

The viscosity in our model is dependent on grainsize, temperature, and stress. Following Landuyt et al (2008), we use the inverse grainsize or fineness A . We use the inverse grainsize (fineness) for the sake of convenience. The non-dimensional viscosity in a composite rheology form is (see Appendix A)

$$\eta = e^{\frac{E_f}{\Theta + \Theta_s}} - \frac{E_f}{1 + \Theta_s} A^{-m} \Sigma \quad (4)$$

where E is the dimensionless activation energy, Θ_s is the surface temperature, exponent m controls the grainsize-dependence of viscosity and is either 2 or 3, depending on the mode of grain diffusion, and

$$\Sigma = \frac{1 + \left(\frac{\sigma}{\sigma_{Tr}}\right)^{n-1}}{1 + \left(\frac{\sigma}{\sigma_T}\right)^{n-1}} \quad (5)$$

where σ is the 2nd invariant of the stress tensor, exponent n governs the stress dependence, σ_r is a reference far-field background stress, σ_T is the transition stress at which strain rates from diffusion and dislocation creep are equal (Hirth and Kohlstedt, 2003), and σ_{Tr} is a reference far-field background transition stress (see Appendix A).

The transition stress σ_T is dependent on fineness, where large fineness corresponds to high transition stress. Dislocation creep is the dominant deformation mechanism where the stress is larger than the transition stress, and diffusion creep is the dominant deformation mechanism where the stress is less than the transition stress. Eq. (4) can be used for either purely diffusion creep (Newtonian) with $n = 1$, or composite rheology with diffusion and dislocation creep (non-Newtonian) with $n = 3.5$ (see Appendix A for full derivation). In Newtonian models, viscosity is dependent only on fineness and temperature. In non-Newtonian models, viscosity is dependent on temperature, fineness, and stress.

There are two limiting behaviors in non-Newtonian rheology: in the diffusion creep limit, $\sigma < \sigma_T$, and the viscosity becomes independent of stress; in the dislocation creep limit, $\sigma > \sigma_T$, and viscosity becomes independent of fineness (see Appendix A). The reference transition stress governs the stress dependence of viscosity in non-Newtonian models, where a small reference transition stress corresponds to small transition stress, and hence strong nonlinear weakening and sensitivity to stress in viscosity.

Grainsize depends on grain damage and healing that is also controlled by temperature (Foley and Bercovici, 2014; Mulyukova and Bercovici, 2017a). The nondimensional equation for fineness evolution (see Appendix A) is

$$\frac{dA}{dt} = D\Psi - HhA^p \quad (6)$$

where the exponent p is set to either 3 or 5 in this study, D and H are nondimensional damaging and healing parameters that are defined in Appendix A, Ψ is the deformational work, and h is the temperature-dependent healing. h and Ψ are given by

$$h = e^{-\frac{E_h}{\Theta + \Theta_s}} + \frac{E_h}{1 + \Theta_s} \quad (7)$$

$$\Psi = \dot{\varepsilon}\sigma = \frac{\sigma^2}{\eta} = \dot{\varepsilon}^2\eta \quad (8)$$

where E_h is the grain growth activation energy. While a large

Table 1

Values which nondimensionalize and rescale all the relevant variables.

Parameter	Reference value
ρ_r	3400 kg/m ³
g	9.8 m/s
α	$3 \times 10^{-5} \text{ K}^{-1}$
ΔT	1300 K
d	1500 km
κ	$10^{-6} \text{ m}^2/\text{s}$
η_r	10^{21} Pa s
A_r	100 m^{-1}
σ_0	440 Pa
σ_r	0.44 MPa
σ_{Tr}	1–10 MPa
E, E_h (Newtonian)	120 kJ/mol
E, E_h (non-Newtonian)	300 kJ/mol

deformational work Ψ or damaging parameter D enhances grainsize reduction (i.e., increase of fineness A), a large healing parameter H enhances grain growth (i.e., decrease of fineness A). The choice of $p = 3$ or 5 governs whether the mineral assemblage is monomineralic ($p = 3$) or polymimetic ($p = 5$), which empirically leads to grain growth with the square root of time, or with the quartic root of time, respectively (Foley et al, 2012).

The values of D and H are determined by scaling factors (Appendix A, Table 1), and in conjunction with the deviatoric stress level, control the relative timescales on which damage and healing of grains occur. From the marginally constrained scaling factors f , the damage partitioning coefficient (10^{-6} – 10^{-1}), and A_r , the reference fineness (10^1 – 10^3), the damage parameter D may vary from 10^{-7} – 10^1 , and the healing parameter H may vary from 10^1 – 10^{15} . In the present study, we choose a subset from the range of D and H for which damage dominates over healing (i.e., the timescale on which damage occurs is more rapid than that for healing). This guarantees that the slab always develops a necking instability and detaches. To isolate the effects of changing the rate of damage, we choose a constant value of $H = 2.3 \times 10^5$ for all models and vary the damage parameter $D = 4.4 \times 10^{-4}$ – 4.4×10^{-2} . The damage parameter values used this study are consistent with those in Foley et al, 2012, whereas the healing parameter values used here are larger (compare with $D = 10^{-3}$ – 10^{-1} , $H = 8.35 \times 10^3$ in Foley et al, 2012).

2.2. Model characteristics

We compute a series of models with varying D , m and p to demonstrate the dynamics of damage, the timescales on which a necking instability develops, and the timescale on which decoupling of the slab from the overlying plate occurs. We consider a thermal convection model in a 2-D Cartesian box with an aspect ratio of 2, which extends to a depth of 1500 km (Table 1). The boundary conditions are free-slip on all four sides. The temperature is fixed at 0 at the surface and 1 at the bottom, while the vertical sidewalls are insulating. The initial temperature field is given by a thermal boundary layer at the surface, and a subducted slab with the mean temperature of the surface and ambient mantle that hangs from the lithosphere (Fig. 1). The dimensional thickness of the thermal boundary layer (i.e., lithosphere) and subducted slab is 150 km. The governing equations of mantle convection (i.e. Eqs. (1)–(3)) are solved using the finite element code Citcom (Moresi and Solomatov, 1995). The models use 128 horizontal and 64 vertical elements which gives a 23 km resolution, there are 16 particles in each element, and the time step is set by the CFL condition.

The equation for evolution of fineness (i.e. Eq. (6)) is similar to the equation of composition conservation in mantle convection studies, except for the source terms on the right-hand side. While Eq. (6) has been solved using a field-based method (Foley and Bercovici, 2014),

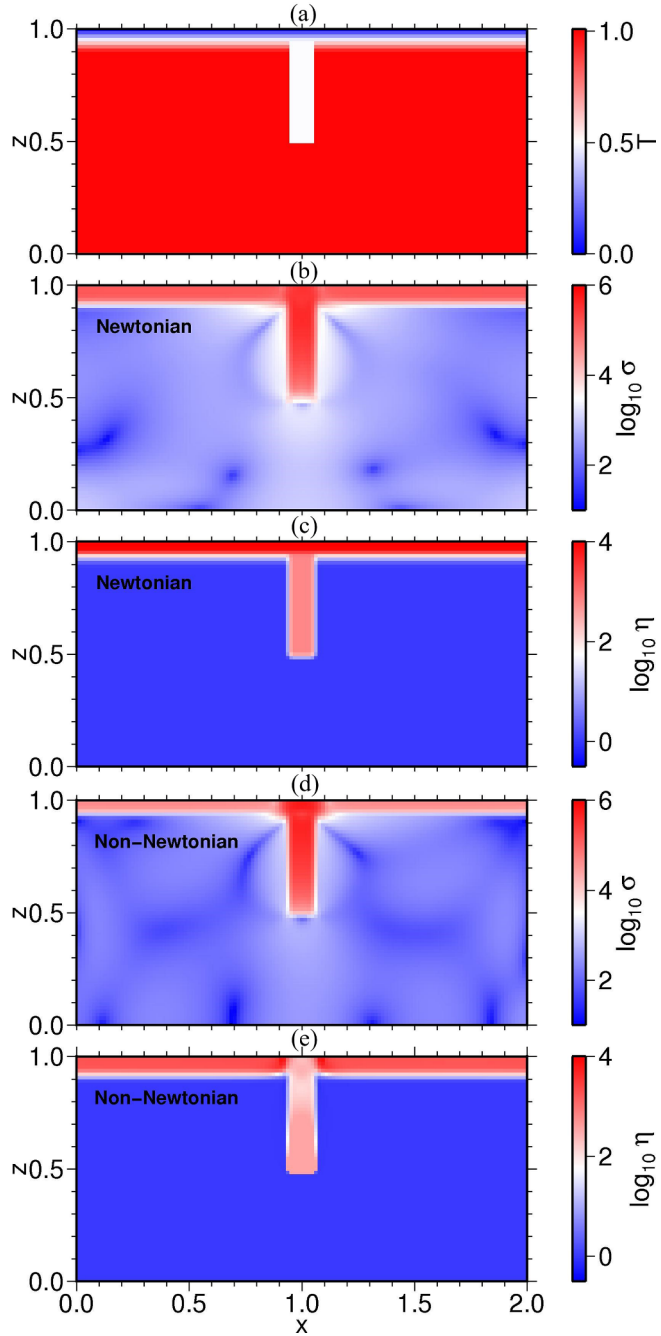


Fig. 1. Initial dimensionless temperature (a); stress (b) and viscosity (c) for Newtonian models; stress (d) and viscosity (e) for non-Newtonian models with reference transition stress $\sigma_{Tr} = 5 \text{ MPa}$.

here it is solved using a particle method (e.g., Tackley and King, 2003), similarly to how the compositional field is modeled in mantle convection studies (McNamara and Zhong, 2004). In our particle-based method, the fineness field A is represented by a distribution of particles. To update the field, we update particle positions from the flow velocity using a predictor-corrector scheme. We also consider the effects of damage and healing on the field. The particle advection scheme used here is the same as in McNamara and Zhong (2004), and Zhong et al. (2008), but the incorporation of the source terms which produce damage and healing is newly implemented for this study.

Consider that at time $t = t_0$, the flow velocity is \mathbf{u}_0 and fineness field A_0 is defined by a distribution of particles at coordinates \vec{x}_0^i for each particle i . To solve the updated fineness field A_1 at the next time-step

$t_1 = t_0 + dt$, we first update the particle's positions using a predictor-corrector scheme (Zhong et al., 2008). The source terms of Eq. (6) depend on temperature and the rate of deformational work. These quantities are computed on the grid and interpolated onto the particles using shape functions of the finite elements. The interpolated quantities are held constant while the fineness field is being updated, using a second order Runge-Kutta scheme, as follows

$$\frac{dA_{i1g}}{dt} = D\Psi_{i1} - Hh_{i1}A_{i0}^p \quad (9)$$

$$dA_{i1g} = dt \frac{dA_{i1g}}{dt} \quad (10)$$

where the subscript g marks the first order approximation of the updated rate of change and value of fineness. We then compute the second-order accurate rate of change, and use it to compute the fineness of each tracer at the following time-step

$$\frac{dA_{i1}}{dt} = D\Psi_{i1} - Hh_{i1}\left(A_{i0} + \frac{1}{2}dA_{i1g}\right)^p \quad (11)$$

$$A_{i1} = A_{i0} + dt \frac{dA_{i1}}{dt} \quad (12)$$

The fineness field is projected from particles onto the grid to determine the viscosity at the grid nodes, where it is used to solve the momentum equation. This is similar to how the composition is projected from particles to the grid (Zhong et al., 2008). The main benefit of using the particle method is to reduce the numerical diffusion and dispersion errors. However, the field-based method can readily employ a solver for the energy equation to evaluate fineness evolution, which is already implemented in any convection code.

Considering the fineness field A is solved at particle locations and projected onto the grid, the question arises as to how the work term, which evolves the particle fineness, can best be evaluated. The method we employ in this study is to solve deformational work directly from conservation of momentum (i.e. on the grid), and project onto particles. Different particles accommodate different amounts of strain according to the linear interpolation of the fields onto the particle location. Another option, however, is to allow the particle-based fineness to dictate the work term at each particle location. In this latter method, the particle fineness introduces nonlinear variation in deformational work from one particle to the next. This is then accompanied by the linear interpolation of temperature, and stress or strain rate, since these parameters are only resolved down to the grid scale. We choose not to employ a particle-based definition of work because temperature, stress and strain rate can vary only linearly at the particle scale in our model (as dictated by the linear shape functions), and hence prefer for work to also vary only linearly at the particle scale (refer to Appendix B for more detailed discussion).

Finally, we find that using a Newton-method iterative solver to compute viscosity significantly improves convergence of the non-linear solutions of the momentum Eq. (2) in the composite rheology models. More commonly, non-Newtonian rheology models employ a method in which the stress (or strain rate and viscosity) from the previous iteration is used to update the viscosity. However, we find that such implementation often leads to relatively slow convergence for the non-linear iterations, and hence use stress from the previous time-step to predict the initial guess for a Newton-method root solver.

We modify the stress-dependent term in the viscosity Eq. (4) by decomposing stress as strain rate multiplied with viscosity, $\sigma = \eta \dot{\epsilon}$, and rearrange the modified viscosity equation with a function $f(\eta)$:

$$f(\eta) = \eta^n \left(\frac{\dot{\epsilon}}{\sigma_T} \right)^{n-1} + \eta - A^{-m} e^{\Theta + \Theta_S} \frac{E_f}{1 + \Theta_S} \left(1 + \left(\frac{\sigma_r}{\sigma_{Tr}} \right)^{n-1} \right) \quad (13)$$

The root of this non-linear equation $f(\eta) = 0$ can be solved iteratively for η using the Newton's method as

$$\eta_i = \eta_{i-1} - \frac{f(\eta_{i-1})}{f'(\eta_{i-1})}, \quad (14)$$

where i denotes the Newton-method iteration, and

$$f'(\eta) = n\eta^{n-1} \left(\frac{\dot{\epsilon}}{\sigma_T} \right)^{n-1} + 1. \quad (15)$$

This procedure is applied to the viscosity calculation for each Gaussian point of every element. With this implementation, the stress is always consistent with strain rate and viscosity on the present time-step (rather than lagging by one time-step). We find that this implementation significantly improves convergence of the nonlinear iteration for flow velocity.

3. Results

We calculate a series of models to understand the effects of specific rheological parameters on the degree of dynamic weakening, and the timescales on which a necking instability and slab detachment develop. Each case is run until whichever arises first of the following cutoff criteria: viscosity contrasts reach a few orders of magnitude across a single element, or the sinking slab reaches the lower boundary of the domain. We systematically vary only three parameters in our models (D , the damage parameter, m , the exponent which controls grainsize dependence of viscosity, and p , the exponent which controls the grainsize dependence of healing).

We provide two analyses to motivate a systematic exploration of the damage model in [Section 3.1](#), present analysis of fineness, viscosity and stress for two reference cases in the linear rheology regime in [Section 3.2](#) and compare results for different rheology including non-linear rheology in [Section 3.3](#). In [Section 3.4](#), we explore the characteristic timescale on which weakening occurs in numerical models. Finally, we analyze slab decoupling from the lithosphere in [Section 3.5](#).

3.1. Analysis of the model

Before showing numerical modeling results, we present two simple analyses to place limits on grainsize and estimates on weakening timescales. We derive an upper bound in fineness from the steady state solution of the fineness evolution Eq. [\(6\)](#). For models with $m \neq p$ and linear viscosity, the upper bound of fineness is solved by setting $dA/dt = 0$ to give

$$A_{UB} = \left(\frac{D\sigma^2}{H} \right)^{\frac{1}{p-m}} \quad (16)$$

This equation predicts a maximum fineness dependent on the deviatoric stress level, which, through its effect on the rheology [\(4\)](#), has implications for whether detachment of the slab can occur.

When $m = p$, $dA/dt=0$ yields

$$D\sigma^2 - H = 0 \quad (17)$$

which predicts no steady state fineness, but rather three distinct damage modes depending on stress, σ . For $D\sigma^2 > H$, damage occurs, for $D\sigma^2 = H$, fineness is in steady state, and for $D\sigma^2 < H$ healing occurs. Since $m = p = 3$ produces a singular steady state (i.e. has no limit on how much fineness can increase), these cases may not be physical. We thus predict two distinct damage regimes: one in which fineness is limited by an upper bound, given by Eq. [\(16\)](#), and the other in which fineness can increase indefinitely.

When $m = p = 3$ for linear rheology, it is also possible to derive a simple analytic solution of fineness as a function of time if we assume constant stress. We treat the fineness evolution Eq. [\(6\)](#) as a separable, first-order, ordinary differential equation to solve for fineness as a function of time,

$$A(t) = (A_0^{-2} - 2h(D\sigma^2 - H)t)^{-\frac{1}{2}}, \quad (18)$$

where A_0 is the initial fineness (i.e. $A_0 = 1$). Substituting $A(t)$ from Eq. [\(18\)](#) into the viscosity Eq. [\(4\)](#) with $n = 1$ leads to viscosity as a function of time,

$$\eta(t) = \left(\eta_0^{\frac{2}{3}} - 2h^{\frac{1}{3}}(D\sigma^2 - H)t \right)^{\frac{3}{2}}, \quad (19)$$

where η_0 is the initial viscosity. Solving for the time at which viscosity becomes diminishingly small or equals zero (i.e., $\eta(t_c) = 0$) gives

$$t_c = \frac{\eta_0^{\frac{2}{3}}}{2h^{\frac{1}{3}}(D\sigma^2 - H)}. \quad (20)$$

This time, t_c , can be viewed as a characteristic weakening time over which the viscosity is reduced significantly due to damage. If we take $D\sigma^2 \gg H$ in the damage-dominated models we explore, Eq. [\(20\)](#) becomes

$$t_c = \frac{\eta_0^{\frac{2}{3}}}{2D\sigma^2 h^{\frac{1}{3}}}. \quad (21)$$

The analytic characteristic weakening time predicts an inversely-proportional linear relationship between t_c and D . For $m \neq p$, analytic expressions for the characteristic times are not readily derived. We expect that the characteristic time for a necking instability to develop will be predicted by Eq. [\(21\)](#) for models with the same damage parameter D , and reflect slight variations depending on the choice of m and p , which we will test in the following calculations. Since the upper bound in fineness (Eq. [\(16\)](#)) depends on m and p , the slab is expected to detach more slowly in models with smaller m and larger p due to a smaller upper bound in fineness and more limited damage. As to be discussed later, we will define characteristic weakening times for our numerical models based on either how viscosity or stress is reduced in the slab and compare the results with that from Eq. [\(21\)](#).

3.2. Reference cases with linear rheology

Here, we describe the behavior of weakening of the slab in two reference cases 1a and 1b, with linear rheology ($n = 1$) to build an understanding of how variation of the rheological parameters m and p affects the rate of damage, the necking process, and to test against the analytic predictions. For all linear cases, the initial non-dimensional viscosity is 10^3 in the slab, 10^4 in the shallow lithosphere, and 1 in the ambient mantle due to the choice of activation energy ([Table 1](#)) ([Fig. 1c](#)). The non-dimensional stress is initially high (10^5) in the slab and lithosphere due to the negative buoyancy of the slab. Far away from the slab, the stress is low (10^2 , [Fig. 1b](#)).

In case 1a, the rheological parameters are $D = 4.4 \times 10^{-4}$, $H = 2.3 \times 10^5$, and $m = p = 3$. Case 1a is run until the viscosity contrasts become sufficiently large to make convergence of the velocity difficult. The results of viscosity, stress, temperature and fineness are presented at 3 different instants ([Fig. 2a–c](#)). As the flow evolves, damage is concentrated most significantly in the neck, and manifested as high fineness and reduced viscosity in that region ([Fig. 2a and b](#)). Fineness increases along the boundary of the slab where shearing occurs. The necking instability develops where stresses are highest. The slab begins to thin and elongate, and deformation produces a positive feedback with damage such that the slab starts to sink in the mantle. Stress decreases in the slab and overlying lithosphere as the slab decouples from the lithosphere at later time ([Fig. 2c](#)). Note that although the core of the slab shows high viscosity due to its low temperature, a large region surrounding the slab has a very small viscosity as a result of reduced grain size ([Fig. 2c](#)). Also note that the re-normalized times by characteristic weakening time t_c are used in [Fig. 2](#), and $t_c = 1.2 \times 10^{-5}$ in its dimensionless form for case 1a is defined by stress evolution in the neck as to be discussed below. We renormalize using the characteristic weakening time to highlight the different phases of damage in the neck.

To analyze the necking process in each model, we isolate 50 – 150

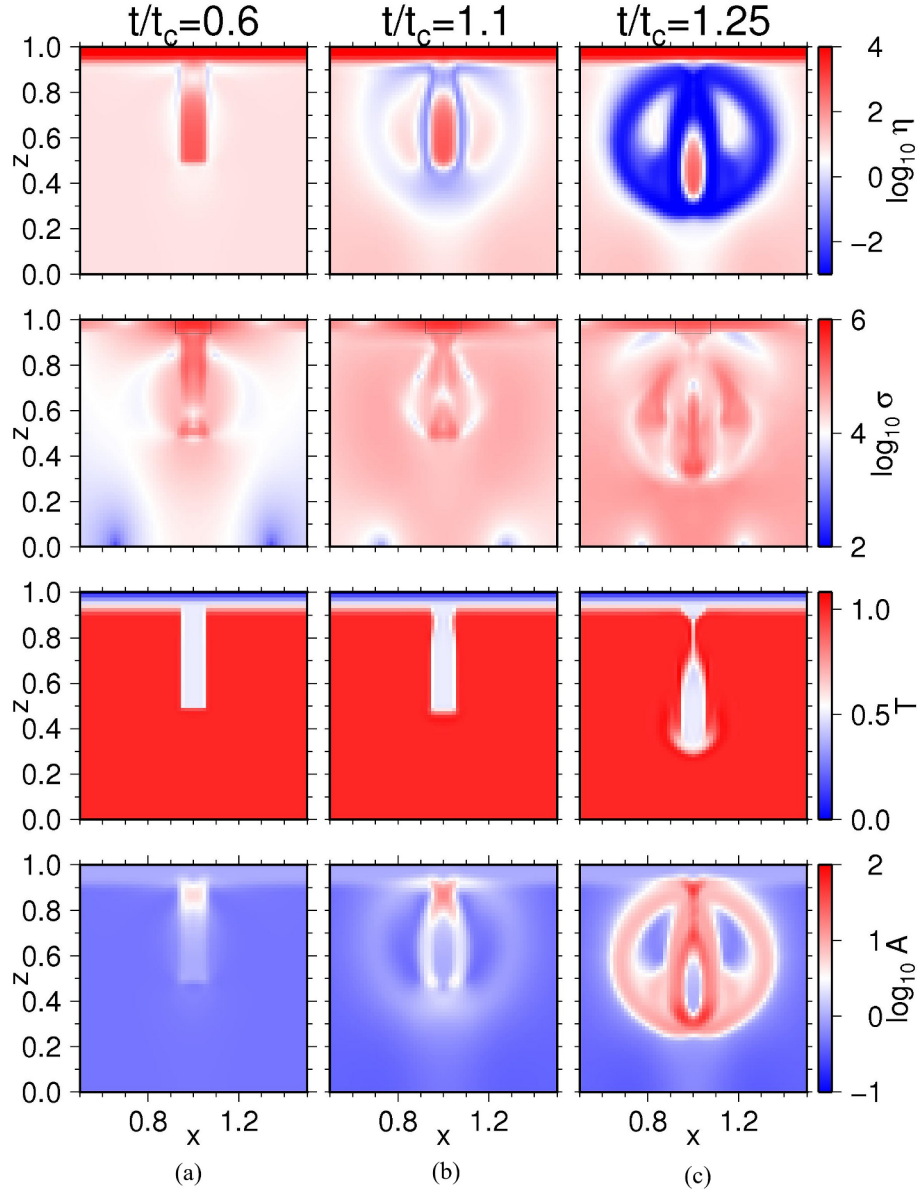


Fig. 2. Dimensionless viscosity, stress, temperature and fineness (from top to bottom) at discrete times (a) 0.6, (b) 1.1, and (c) 1.25 t_c in case 1a ($D = 4.4 \times 10^{-4}$, $m = p = 3$, $t_c = 1.2 \times 10^{-5}$). Time is renormalized by the characteristic weakening timescale defined by numerical results of stress in the slab neck (refer to Fig. 3). Stress inside the rectangles near the surface is averaged to determine the slab-decoupling timescale presented later.

tracer particles by scanning the domain for the greatest viscosity reduction between the initial and final times, and these tracer particles are located in the neck. In the necking region and for case 1a, the rate of increase in fineness is relatively steady until at a point in time when it accelerates steeply (Fig. 3a). The fineness undergoes a factor of 100 total increase from start to finish, while the neck viscosity reduces by approximately 6 orders of magnitude (Fig. 3b). Since the temperature does not change much over this short time scale, the grainsize evolution has a dominant effect on viscosity. Note that the fineness increases indefinitely with no upper bound (Fig. 3a), consistent with the analysis (Eq. (17)) in the last section for $m = p$ as for case 1a. The stress is initially very large ($> 10^5$) but decreases for the majority of the model run before becoming relatively steady (Fig. 3c). A few tracers in the necking region are associated with a plunge in stress at the very end of the model run. This is an example of convergence issues which force us to terminate the model run (note how closely spaced the time-steps become).

The characteristic weakening timescale captures the time over

which the viscosity and stress in the neck experiences a rapid, initial drop, after which the slab begins to sink (the process described here is also relevant to the plunge which follows the buildup of stress in a passive margin as explored by Mulyukova and Bercovici (2017b)). For our numerical models, we define the characteristic weakening time t_c as the time of minimal variation with time in either viscosity or stress after initial, rapid reduction (i.e. enters approximate steady state). In models with $m = p = 3$ (i.e., case 1a), since the fineness or viscosity is not bounded (Fig. 3a and b), we use the stress evolution to define t_c ($t_c = 1.2 \times 10^{-5}$ from triangles in Fig. 3c), while for other models $m \neq p$ where the viscosity reaches a steady state value, time evolution of either stress or viscosity may be used to define t_c , as to be discussed later. For case 1a, the characteristic weakening time approximates the timescale on which the necking instability develops (Figs. 2 and 3). Note that $t_c = 1.9 \times 10^{-5}$ for case 1a as predicted from Eq. (21) using averaged stress in Fig. 3, similar to that determined numerically.

To test the robustness of the results, we re-compute case 1a with doubled spatial resolution (from 128×64 to 256×128 elements), and

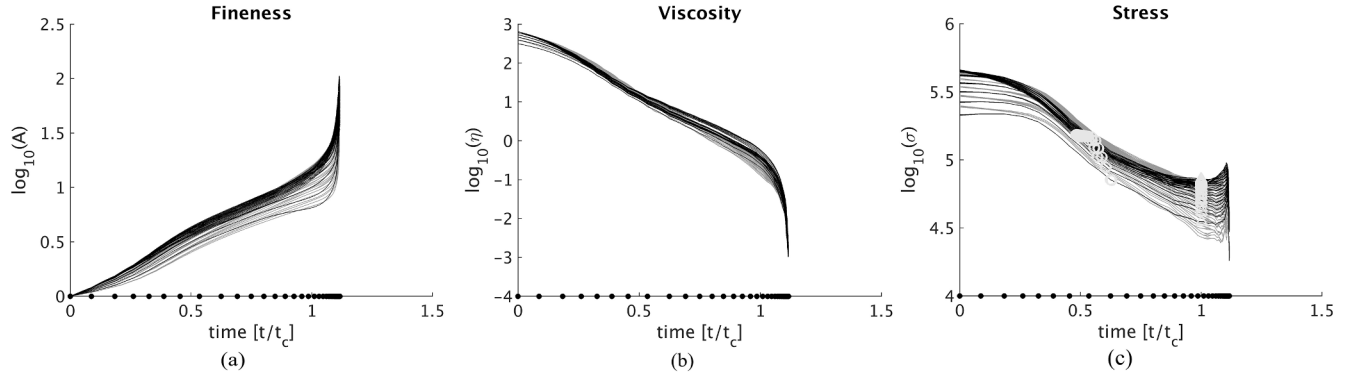


Fig. 3. Dimensionless fineness (a), viscosity (b), and stress (c) for 72 of the most significantly weakened particles in case 1a (black). All tracers plotted here are located in the slab neck. The triangles superposed on (c) indicate the time of minimal slope after a period of rapid reduction (i.e. the numerical characteristic weakening timescale used to renormalize time). The circles mark the time at which stress has reduced by a factor of 3 (i.e. the decoupling timescale in Bercovici et al., 2015). The black ticks on the time axis mark every 0.1 time step, and time is renormalized by the characteristic weakening timescale for case 1a ($t_c = 1.35 \times 10^{-5}$). We include for comparison the fineness (d), viscosity (e), and stress (f) for a higher resolution test of case 1a in gray (double spatial, and a factor 10 times the temporal resolution). The characteristic weakening timescale $t_c = 1.17 \times 10^{-5}$ in the high resolution test.

Table 2
List of model formulations and run times.

Case	Rheology	σ_{Tr} [MPa]	D	m	p	Time steps	Elapsed time
1a	Linear	–	4.4×10^{-4}	3	3	710	1.51×10^{-5}
1b	Linear	–	4.4×10^{-4}	2	5	5000	1.31×10^{-4}
1c	Linear	–	4.4×10^{-4}	2	3	14,300	4.81×10^{-5}
1d	Linear	–	4.4×10^{-4}	3	5	4000	4.71×10^{-5}
1a _{HR}	Linear	–	4.4×10^{-4}	3	3	4600	1.31×10^{-5}
2a	Linear	–	4.4×10^{-3}	3	3	1950	7.61×10^{-7}
2b	Linear	–	4.4×10^{-3}	2	5	200,000	3.20×10^{-5}
2c	Linear	–	4.4×10^{-3}	2	3	4700	1.82×10^{-6}
2d	Linear	–	4.4×10^{-3}	3	5	9300	1.14×10^{-6}
3a	Linear	–	4.4×10^{-2}	3	3	2500	9.23×10^{-8}
3b	Linear	–	4.4×10^{-2}	2	5	40,000	3.13×10^{-6}
3c	Linear	–	4.4×10^{-2}	2	3	2300	1.57×10^{-7}
3d	Linear	–	4.4×10^{-2}	3	5	1950	7.28×10^{-8}
4a	Non-linear	5.0	4.4×10^{-4}	3	3	230	2.03×10^{-4}
4b	Non-linear	5.0	4.4×10^{-4}	2	5	1950	3.55×10^{-4}
4c	Non-linear	5.0	4.4×10^{-4}	2	3	1250	3.26×10^{-4}
4d	Non-linear	5.0	4.4×10^{-4}	3	5	2400	2.94×10^{-4}
4e	Non-linear	1.0	4.4×10^{-4}	2	5	5000	2.71×10^{-5}
4f	Non-linear	10.0	4.4×10^{-4}	2	5	850	6.92×10^{-4}

10 times the temporal resolution as case 1a_{HR} (Table 2, Fig. 3). The higher resolution calculation confirms the robustness of model results in case 1a. We find that the spatial pattern and extent of weakening are well matched, although the high-resolution case evolves more rapidly due to increased localization (a time lag of $0.1t_c$ resolves any significant differences). The rate of deformation is dependent on resolution (Hillebrand et al., 2014), but the influence is weak compared to that of the damage parameter D , as the following models will demonstrate.

Note from Fig. 2c that due to numerical error, the temperature exhibits an overshoot of the maximum expected ($T = 1.0$) by up to several percent in halos surrounding the slab. To examine whether the temperature-overshoot would affect the general results, we re-compute case 1a in which the temperature is filtered to limit $T \leq 1.0$ and verify differences are negligibly small compared to the original results in case 1a.

Case 1b is formulated identically to case 1a, except $m = 2, p = 5$ (compared to $m = p = 3$). Results for viscosity, stress, temperature and fineness are plotted at discrete times $t/t_c = 1.3, 7.6$, and 11.7 in Fig. 4a–c, respectively. The slab detachment process is similar to that in case 1a. For case 1b, t_c is 1.2×10^{-5} and 1.5×10^{-5} , based on stress and viscosity evolution, respectively (Fig. 5d and 5g), which is the similar to that for case 1a. Damage is less localized, and the rate of damage is slower in case 1b compared to case 1a.

For case 1b, damage in the necking region is rapid while $t/t_c < 1$, but for $t/t_c > 1$, damage plateaus, and when $t/t_c > 1$, healing begins to

compete with and dominate over damage due to the effects of increased temperature in the slab neck (i.e., the slab neck thins and exchanges heat with the ambient mantle) (Figs. 4b, c, and 5a). The viscosity in the slab neck reaches a relatively steady value after t_c similar to the fineness, and then decreases at a slow, steady rate consistent with steadily increasing temperature in the neck (Fig. 5d). The slab neck stress decreases rapidly by a factor of 1.5 in the first t_c , plateaus, and then at $7t_c$ decreases rapidly again as deformation in the elongated neck subsides (Fig. 5g).

The rheological evolution of cases 1a and 1b fall into two distinct damage regimes. Most importantly, the fineness and viscosity evolve with increasing rate and with no sign of abatement in case 1a with $m = p = 3$ (Fig. 3), while in case 1b with $m \neq p$ the fineness and viscosity quickly produce relatively steady values (Fig. 5a and d). This is consistent with the analysis on an upper bound in fineness as predicted by Eqs. (16) and (17). We use this dichotomizing feature to describe the remaining linear models. For case 1b, the upper bound of fineness as predicted by Eq. (16) using stress for case 1b (Fig. 5g) is similar to model fineness after t_c (black versus gray curves in Fig. 5a), showing the validity of our analysis.

3.3. Models with different rheological parameters

We can now extend this analysis to the other formulations of rheology. Based on the prediction of steady state fineness, we divide all cases into two groups: those with $m = p = 3$, and those with $m \neq p$. Cases with $m = p = 3$ are grouped as case-a, and for cases with $m \neq p$, three different combinations of m and p are considered: $m = 2, p = 5$ are grouped as case-b, $m = 2, p = 5$ as case-c, and $m = 2, p = 5$ as case-d (Table 2). For each group, three different damage parameters $D = 4.4 \times 10^{-4}, 4.4 \times 10^{-3}$ and 4.4×10^{-2} are also considered and are grouped as case 1, 2, and 3, respectively, in the linear regime (e.g., cases 1a and 1b considered earlier). Non-Newtonian rheology models are grouped as case 4.

3.3.1. Models with different m, p and D

In general, increasing the damage parameter D increases the rate of damage, the total change in viscosity, and produces larger, more localized viscosity contrasts. Exponent m controls grainsize dependence of viscosity (Eq. (4)). Exponent p controls grain healing (Eq. (6)), where systems with larger p typically produce more limited and less rapid damage due to competition from the healing term. Following this trend, all case-a models exhibit the fastest and most significant evolution of damage as they are formulated with $m = p = 3$ and do not have a steady state fineness. All case-b models, formulated with $m = 2, p = 5$,

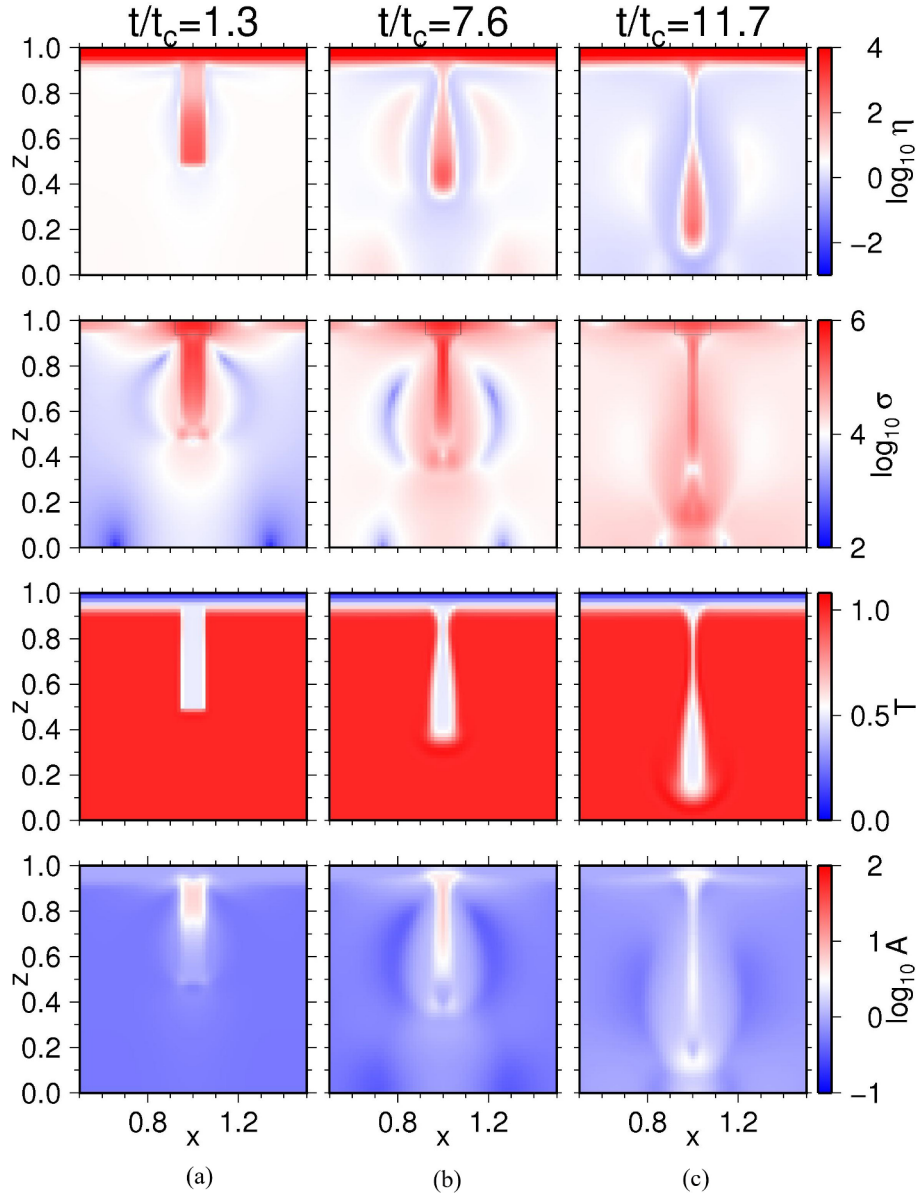


Fig. 4. Viscosity, stress, temperature and fineness (from top to bottom) are plotted at discrete times (a) 1.3, (b) 7.6, and (c) 11.7 t_c for case 1b ($D = 4.4 \times 10^{-4}$, $m = 2$, $p = 5$, $t_c = 1.2 \times 10^{-5}$). Stress inside the rectangles near the surface is averaged to determine the slab-decoupling timescale presented later. Time is renormalized by the characteristic weakening timescale (refer to Fig. 5).

typically exhibit the most limited damage and slowest detachment of the slab.

The combinations of m and p associated with case-c ($m = 2$, $p = 3$) and case-d ($m = 3$, $p = 5$) behave similarly to case-b, because they are formulated with $m \neq p$, and hence have an upper bound in fineness (Eq. (16)). The case-c and case-d models eventually produce a relatively steady value of fineness and hence viscosity (Fig. 5, the middle and right columns). The magnitude of damage in case-c and case-d models is intermediate to case-a and case-b.

The results for linear cases with varying D are similar to those of cases 1a-d, except the timescale on which the slab evolves reduces dramatically with increasing D . We elaborate on the relationship between timescale and D in the following section. For now, the important point is that case-a models evolve differently from case-b, -c, and -d models, because $m = p = 3$ in case-a leads to runaway increase in fineness. Between models with $m \neq p$, the lesser the difference between m and p , the more extensive the damage and more rapid the evolution of the slab (Fig. 5).

3.3.2. Non-Newtonian rheology

Here we describe the effect of non-linear or stress-dependent viscosity. Case 4b differs from case 1b only in having $n = 3.5$ (i.e. non-Newtonian rheology), and a larger viscous activation energy $E = 300$ kJ/mol (compare with 120 kJ/mol in case 1b). We use a larger viscous activation energy for non-Newtonian models to be consistent with geodynamic models of the Pacific upper mantle and lithospheric seismic structure (van Hunen et al., 2005). Significantly higher viscous activation energy increases viscosity in cold regions (i.e. the slab), which is partially balanced by stress-induced weakening. The degree of weakening is controlled by the value of the reference far-field transition stress σ_{Tr} (Eqs. (4), (5) and Appendix A). In cases 4a-d, σ_{Tr} is set to 5 MPa, which allows for stress-induced weakening to reduce the slab viscosity to as low as 25% of that in the Newtonian model, despite higher activation energy. We constrain the viscosity below the lithosphere ($z = 0.9$) in non-Newtonian models to be equal to or less than the slab viscosity from Newtonian models.

Results for viscosity, stress, temperature and fineness for case 4b are

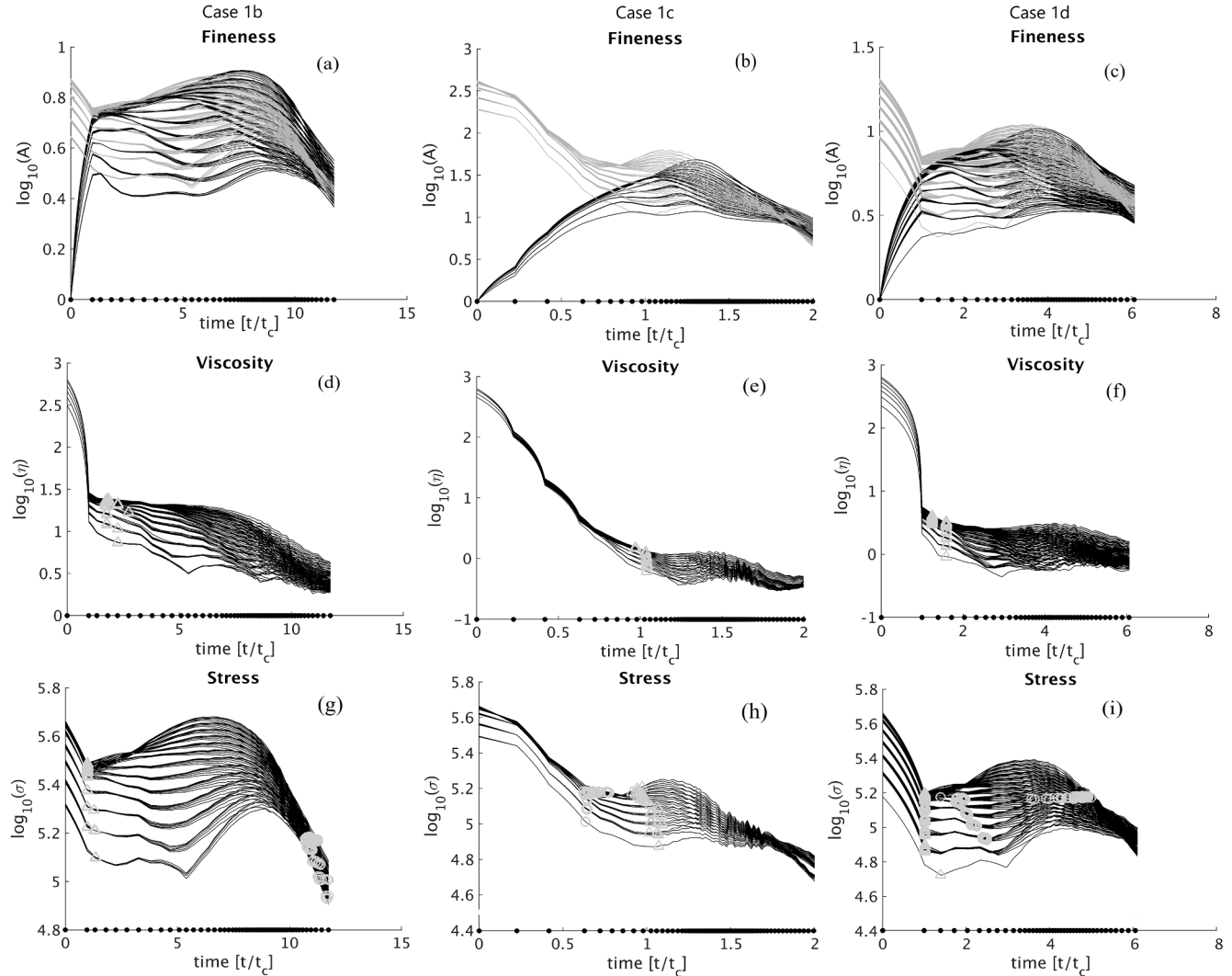


Fig. 5. Fineness (a–c); viscosity (d–f); and stress (g–i) for 50–150 of the most significantly weakened particles in case 1b (first column), case 1c (second column), and case 1d (third column). The gray curve superposed on the fineness in (a–c) is the analytic upper bound solved by setting $dA/dt = 0$ (Eq. (16)). The triangles superposed on viscosity (d–f), and stress (g–i) indicate the time at which the slope becomes minimal after an initial rapid reduction in viscosity and stress, respectively (i.e. the characteristic weakening timescale). The circles superposed on stress (g–i) mark the time at which stress has reduced by a factor of 3 (i.e. the decoupling timescale in Bercovici et al., 2015). The tracers plotted here are always located in the necking region. Time is renormalized by the characteristic weakening timescale, which is defined by the time at which the slope of stress becomes minimal after the initial rapid reduction. Characteristic weakening timescale $t_c = 1.2 \times 10^{-5}$, 2.4×10^{-5} , 7.8×10^{-6} for case 1b, 1c and 1d respectively.

plotted at discrete (nondimensional) times 1.2×10^{-4} , 3.4×10^{-4} and 3.6×10^{-4} in Fig. 6a–c, respectively. Between 3.4×10^{-4} and 3.6×10^{-4} , the slab precipitously detaches from the lithosphere and falls into the mantle. This is accompanied by rapid reduction of stress and viscosity in the neck (Fig. 7). The stress field in the neck undergoes an order of magnitude reduction (Fig. 6b and c), which is corroborated by the isolated tracers. Non-Newtonian models reproduce the steady state fineness for models with $m \neq p$ in good agreement with the prediction from Eq. (16) (Fig. 7a).

Considering Fig. 7, the viscosity decreases by only one order of magnitude over the first 2×10^{-4} of the elapsed time, despite one order of magnitude increase in fineness and cubic fineness-dependence (i.e., predicts three orders of magnitude decrease in viscosity). This demonstrates that the fineness-dependence of viscosity is damped by high stress. Without stress-dependence of viscosity, viscosity would decrease rapidly and then plateau following the fineness. Similarly, the stress would decrease rapidly and then plateau following viscosity. Non-Newtonian viscosity does not reflect the total increase in fineness until the stress reduces dramatically as the slab detaches and falls into the

mantle (after $t = 2 \times 10^{-4}$).

The total elapsed time is 3.6×10^{-4} for case 4b, compared with 1.2×10^{-4} for case 1b. This demonstrates that even when viscosity in the slab is constrained to be equal to or less than Newtonian models, the addition of nonlinear weakening produces evolution less rapid compared to purely linear weakening. In the limit where stress is large, the viscosity becomes independent of fineness, and so the slab neck remains relatively stronger despite significant fineness evolution.

Case 4e, with a smaller reference transition stress $\sigma_{Tr} = 1$ MPa (but otherwise identical to case 4b), exhibits more extensive and more rapid nonlinear weakening in the slab neck, compared with case 4b. Lower initial viscosity increases the rate of deformation and detachment (e.g., slab detachment occurs at 2.7×10^{-5} in Fig. 8a and b). Case 4f, with a larger reference transition stress $\sigma_{Tr} = 10$ MPa (but otherwise identical to case 4b), has a larger initial viscosity in the slab, and hence evolves more slowly (slab detachment at 6.9×10^{-4} in Fig. 8c and d). As the reference transition stress is increased further, the stress-dependence of viscosity is reduced, and the formulation approaches Newtonian rheology. Newtonian rheology models with increased viscous activation

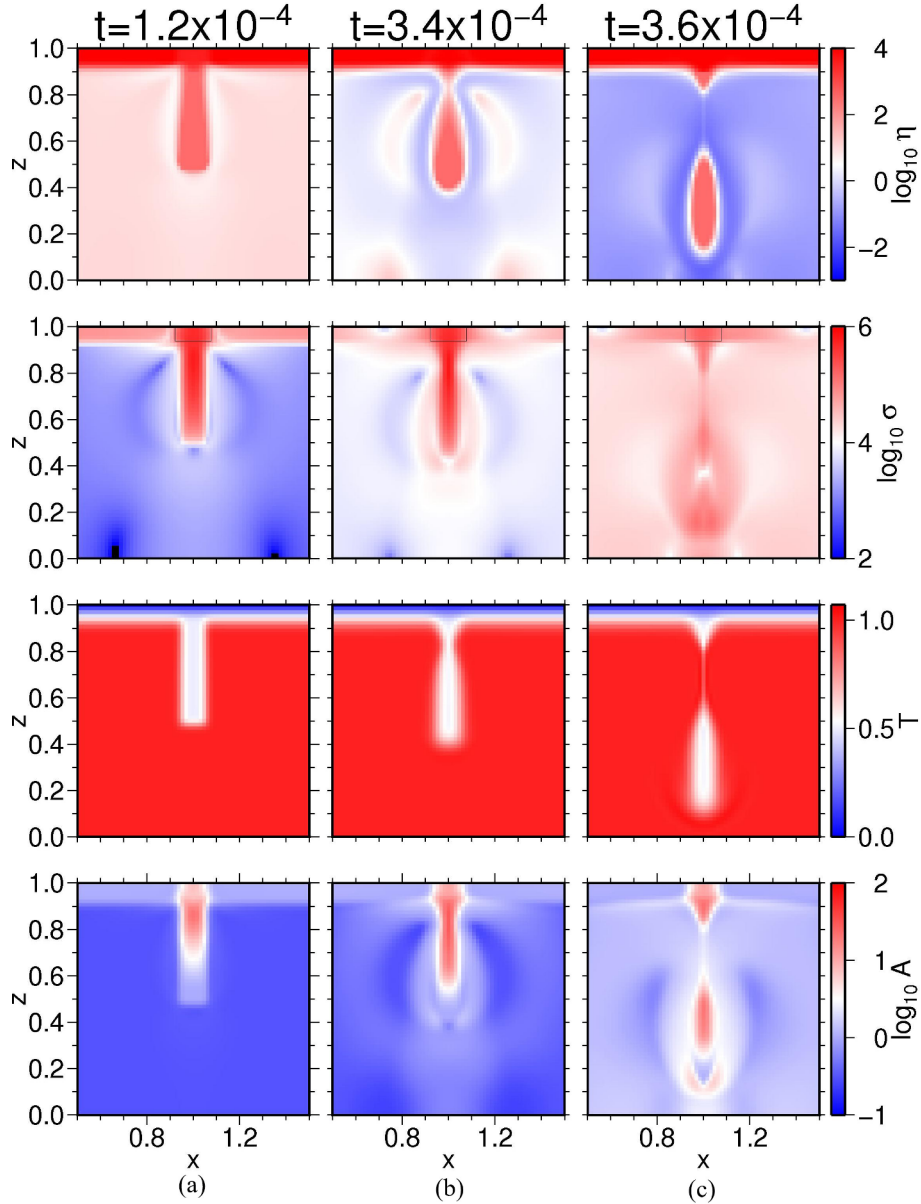


Fig. 6. Viscosity, stress, temperature and fineness (from top to bottom) at discrete nondimensional times (a) 1.2×10^{-4} , (b) 3.4×10^{-4} , (c) 3.6×10^{-4} for nonlinear case 4b ($\sigma_{Tr} = 5$ MPa, $D = 4.4 \times 10^{-4}$, $m = 2$, $p = 5$). Although only 0.2×10^{-4} or 5% of the run time elapses between (b) and (c), the slab evolves very rapidly as it detaches from the surface.

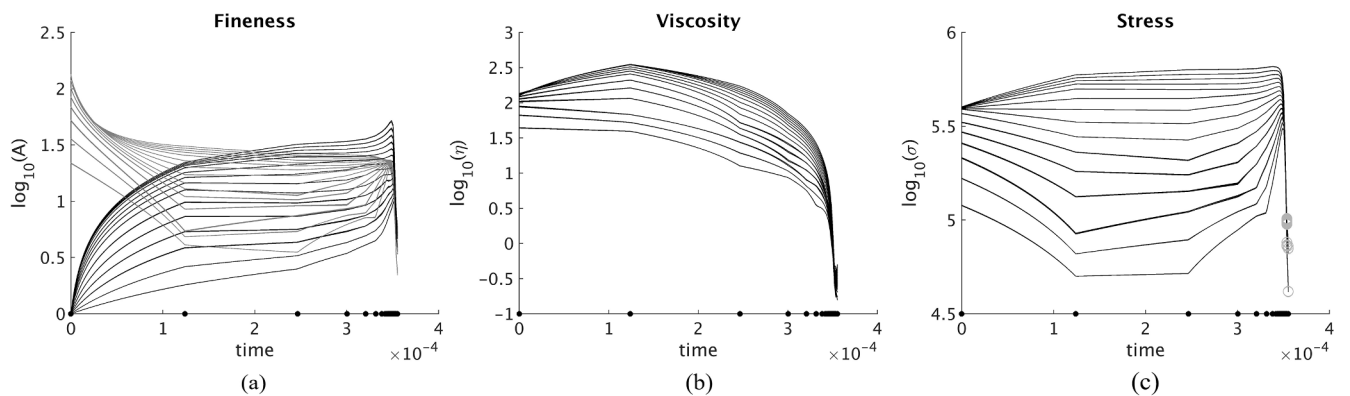


Fig. 7. Fineness (a), viscosity (b), and stress (c) for 39 of the most significantly weakened particles in case 4b. All tracers plotted here are located in the necking region. The dots on the time axis mark every 50th time step. The sharp drop in stress, viscosity and fineness at 3.4×10^{-4} corresponds to the slab descending rapidly in the mantle after it has detached. The gray curves superposed on (a) are the steady state fineness (Eq. (16)). All times are nondimensional and not renormalized, because a characteristic weakening timescale is not evident from the evolution of stress nor viscosity in the neck.

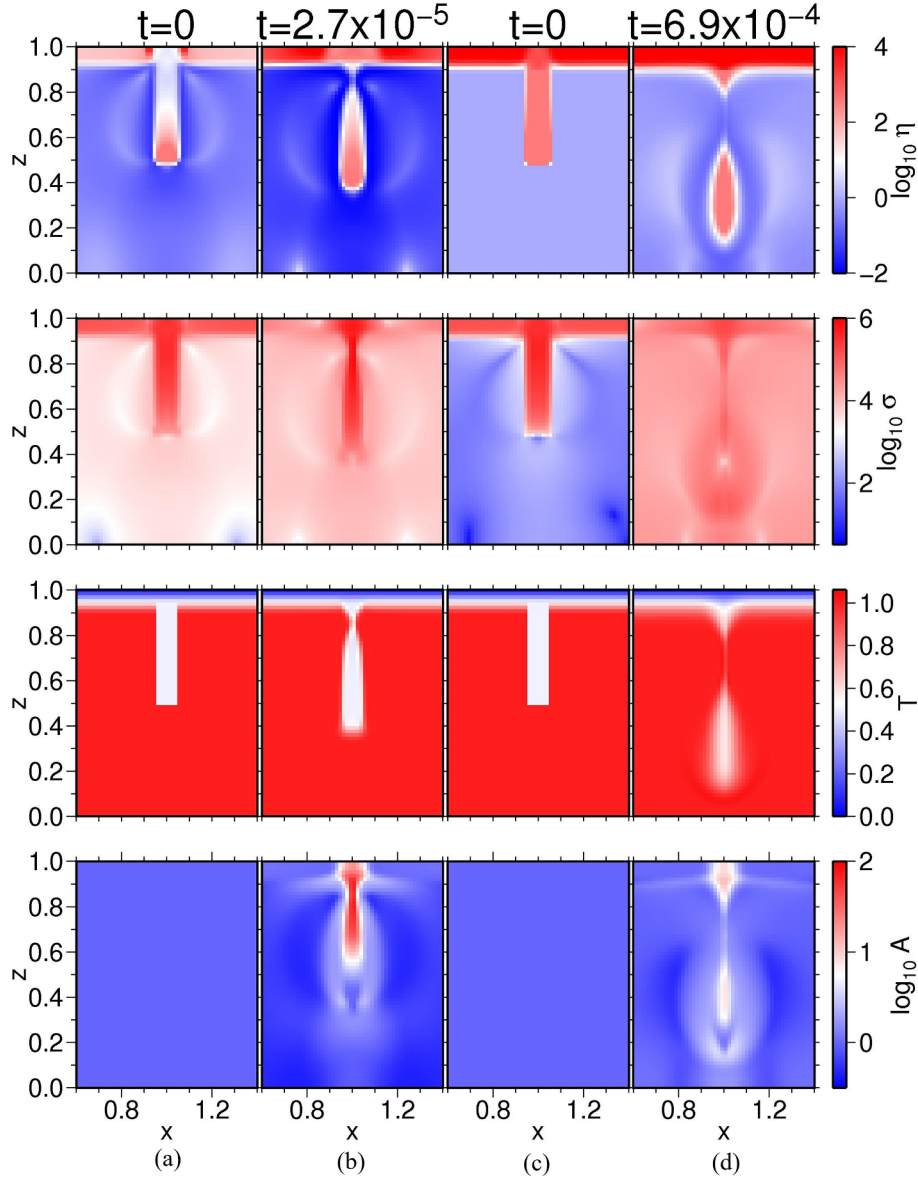


Fig. 8. Viscosity, stress, temperature and fineness (from top to bottom) at discrete nondimensional times (a) 0, and (b) 2.7×10^{-5} for nonlinear case 4e ($\sigma_{Tr} = 1$ MPa), and (c) 0, and (d) 6.9×10^{-4} for nonlinear case 4f ($\sigma_{Tr} = 10$ MPa). For both cases plotted above, $D = 4.4 \times 10^{-4}$, $m = 2$, $p = 5$. The rapid evolution of the slab in case 4e compared to case 4b is caused by a smaller reference transition stress, and increased nonlinear weakening.

energy evolve very slowly (e.g., $40t_c$ for $E = 216$ kJ/mol) due to very high initial viscosity in the slab and lithosphere.

We have computed nonlinear rheology cases ($n = 3.5$) with $\sigma_{Tr} = 5$ MPa, and different m and p as done for linear rheology cases ($n = 1$) (Table 2). The trends in weakening are similar to what we observe in linear cases, where $m = p = 3$ produces runaway fineness, and $m \neq p$ does not. However, we find that the stress and viscosity do not approach a steady value after an initial phase of rapid reduction, despite relatively steady fineness. Rather, the stress remains relatively steady while the slab neck undergoes damage and gradual reduction of viscosity, until the neck is weak enough for the slab to detach. Upon detachment, the stress reduces dramatically, as does the viscosity as it transitions from high-stress limit (fineness-independent) into the low stress-limit (stress-independent). This allows the total increase of fineness to be reflected in the viscosity.

3.4. Characteristic weakening timescale

We compare numerical results with the analytic prediction (Eq.

(21)) in the following. The characteristic weakening timescale measures the time taken to weaken the neck sufficiently for a necking instability to develop. It has important geophysical implications pertaining to slab detachment and abrupt tectonics (e.g., [Bercovici et al., 2015](#)), and is insightful to each rheology. We quantify this timescale as the time taken for viscosity and stress in the neck to reach a relatively steady value.

We find the characteristic weakening timescale is inversely proportional to D , follows a linear trend in log-log scale, and ranges from $6.5 \times 10^{-8} - 2.7 \times 10^{-5}$ (Fig. 9). Characteristic weakening time is mostly controlled by D , while the effect of m and p appears secondary. The numerical viscosity- and stress-based characteristic weakening timescales are similar, and as an example are 1.5×10^{-5} and 1.2×10^{-5} , respectively, for case 1b (Fig. 5d and g). An order of magnitude variation in D produces approximately one order magnitude change in timescale. The timescales defined by numerical results of stress and viscosity are consistent with that predicted by the analytic characteristic weakening timescale. Non-Newtonian models do not as clearly exhibit an initial phase of weakening like the Newtonian models, so we will not include them in this analysis.

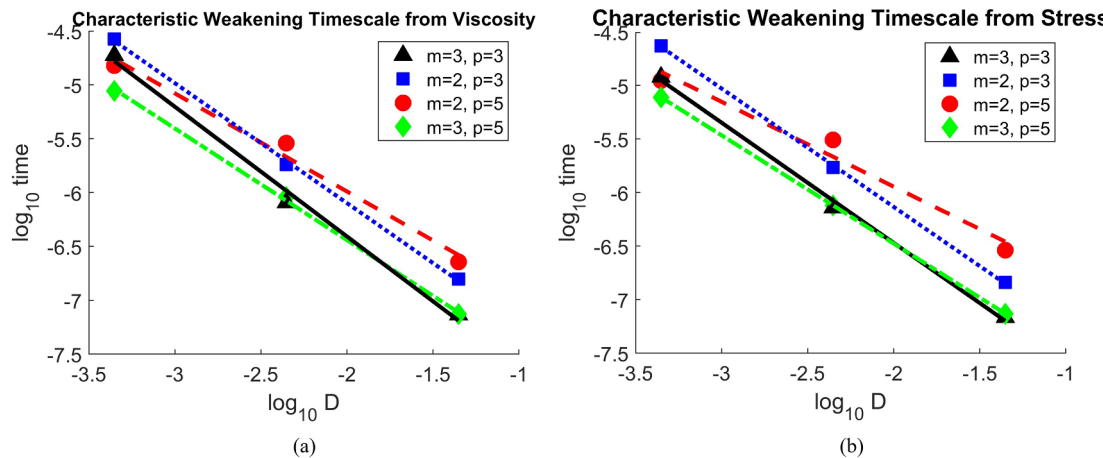


Fig. 9. Nondimensional characteristic timescale based on viscosity (a) and stress (b) in Newtonian-rheology models. For cases with $m = p = 3$, the characteristic weakening timescale defined by viscosity (a) is the analytic solution (Eq. (21)) using the average of stress for the critical tracers in the slab neck.

3.5. Slab decoupling and lithospheric stress response

As the slab neck is weakened by damage, the slab eventually decouples from the lithosphere. Following Bercovici et al. (2015), we can define characteristic timescale for slab decoupling using stress reduction in the slab neck, similar to our characteristic timescale defined in the preceding section. It would be interesting to examine whether the lithospheric stress responds on the same timescale, given that lithospheric stress may be more directly responsible for surface tectonics such as changes in plate motion. In the following, the timescale associated with stress reduction by a factor of 3 in the neck (as in Bercovici et al., 2015) is compared with the timescale associated with stress reduction by a factor of 2 in the lithosphere (this study).

The case-a models ($m = p = 3$) experience gradual reduction in lithospheric stress for the majority of the model run, followed by a sharp drop (Fig. 10a). In case 1a, while stress in the slab decreases by a factor of 3 after $0.5t_c$, appreciable reduction of stress in the lithosphere does not occur until $1.25t_c$. Cases 1c and 1d also exhibit significant lag of stress reduction in the lithosphere relative to stress reduction in the neck (Fig. 10c, d). For case 1b with $m = 2$ and $p = 5$, the decoupling timescales defined by stress in the slab neck and lithosphere are about the same at $\sim 11t_c$ (Fig. 10b).

The decoupling timescale defined by stress in the surface lithosphere is inversely proportional to the damage parameter D , ranging from 9.6×10^{-8} to 1.2×10^{-4} for the linear rheology models, and from 2.9×10^{-4} to 3.5×10^{-4} in nonlinear rheology (Fig. 11). Compared with the timescale to reduce stress in the slab neck by a factor of 3 (i.e., the timescale as in Bercovici et al., 2015), the decoupling timescale defined by surface stress reduction is generally longer for linear rheology (Fig. 11b), but these two decoupling timescales tend to agree with each other for b-cases with $m = 2, p = 5$, and for nonlinear rheology (Fig. 11).

4. Discussion

Rheology that produces dynamic weakening plays an important role in lithospheric deformation and dynamics. Evolution of viscosity due to grain-damage allows localization of deformation, and provides a simple, physical mechanism for rapid weakening. Relevant geodynamical processes may include the decoupling of a subducted slab from the overlying plate, subsequent reorientation of plate-driving forces, abrupt tectonics (Bercovici et al., 2015), collapse of passive margins (Mulyukova and Bercovici, 2017a), and weakening of the deep lithosphere with potential influence on the emergence of plate tectonics (Bercovici and Ricard, 2005, 2012, 2013, 2014, 2016; Ricard and Bercovici, 2009; Bercovici and Skemer, 2017; Mulyukova and

Bercovici, 2017b).

In this study, we investigate the timescale, extent, and spatial distribution of weakening in a subducted slab under the influence of the slab buoyancy. When damage is incorporated with grainsize-dependent viscosity, slabs may quickly detach from the surface by necking instability in both Newtonian and non-Newtonian rheology. The rate and extent of detachment is governed to first order by the damage parameter D . A large damage parameter produces rapid damage, great contrasts in grain fineness and mantle viscosity, and localization of deformation. The viscous activation energy and type of deformation (Newtonian or non-Newtonian) also impose controls on how quickly the slab evolves, where enhanced stress-induced weakening from non-Newtonian rheology increases the rate of deformation, and larger activation energy decreases the rate of deformation by increasing the viscosity at a given temperature. The exponent m governs the fineness-dependence of viscosity and rate of damage, while exponent p governs the rate of healing. An important characteristic of the rheology is whether $m = p$, in which case damage is unbounded, or $m \neq p$, in which case there is an upper bound or steady state in fineness.

In non-Newtonian rheology models, the viscous activation energy is significantly higher. High viscosity is partially balanced by nonlinear weakening to produce slab viscosity equal to or less than Newtonian models. Due to higher viscous activation energy and the high-stress limit of non-Newtonian rheology, in which viscosity becomes independent of fineness, evolution of the slab is slower in non-Newtonian models compared to Newtonian models.

The timescale on which the slab neck reaches approximately steady state in viscosity and stress has significant implications for the dynamics of geophysical systems involving slabs. We find the characteristic weakening timescale t_c , defined by the time at which time variations of viscosity and stress become minimal, is inversely proportional to D . For the sake of comparison with geophysical observations, in this section we rescale time to dimensional time using time scale of $d^2/\kappa = 7.1 \times 10^{-4}$ Myrs in our model. Our results indicate that damage is a rapid process compared to mantle convection and occurs on timescales ranging 0.005–1.9 Myrs (Fig. 9) for linear rheology, and thus is a viable explanation of abrupt tectonic events.

We find that stress reduction in the lithosphere following slab detachment typically occurs on a longer timescale compared to stress in the slab neck, excluding $m = 2, p = 5$, and nonlinear rheology. The rescaled slab decoupling timescale defined using lithospheric stress at the surface ranges from 0.007 to 8.6 Myrs for linear rheology with $D = 4.4 \times (10^{-4} - 10^{-2})$, and 20.7 to 25.0 Myrs for nonlinear rheology with constant $D = 4.4 \times 10^{-4}$. This range overlaps with the timescales associated with abrupt tectonic events, such as the bend in the Emperor-Hawaiian seamount chain. Furthermore, since the grainsize-

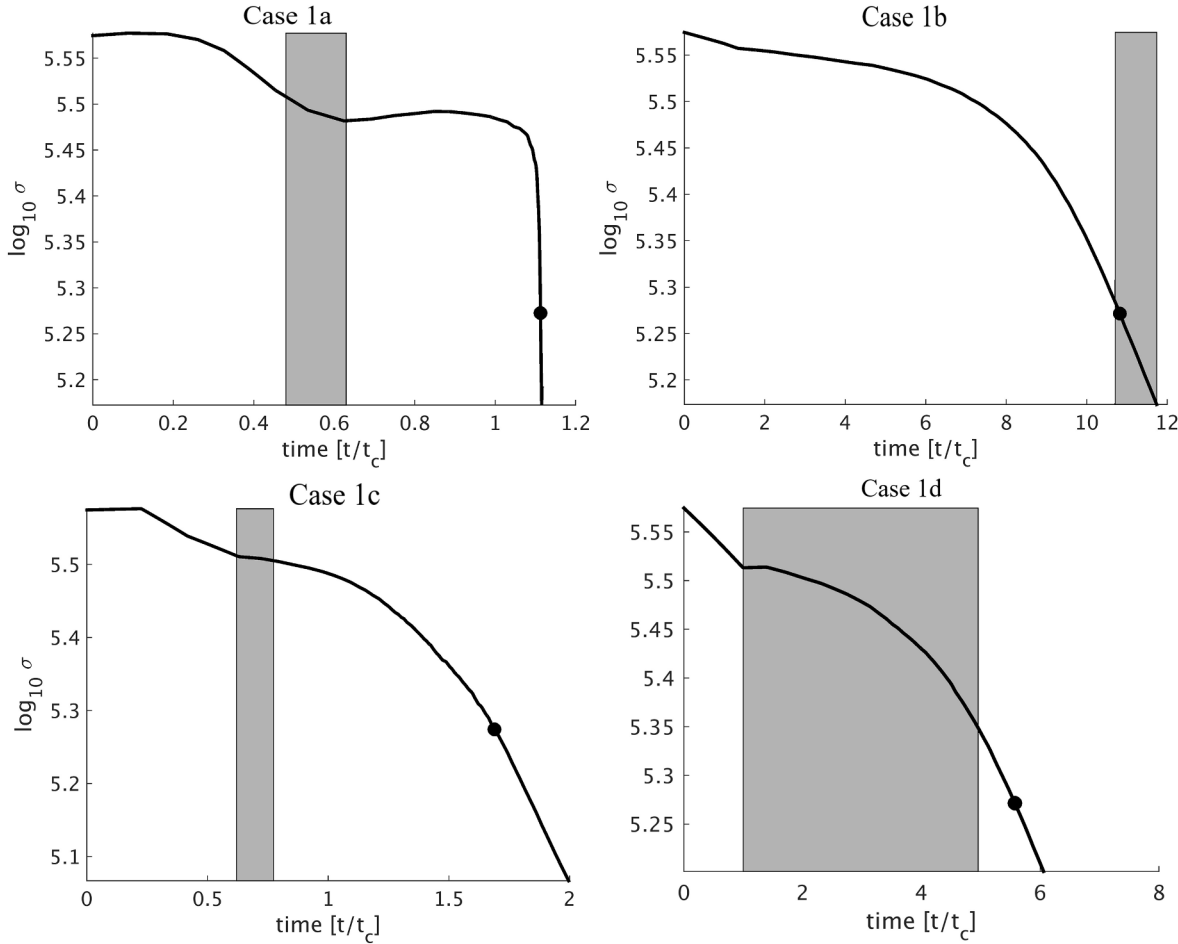


Fig. 10. The average stress in the lithosphere directly overlying the slab for case 1a ($m = p = 3$) (a) and case 1b ($m = 2, p = 5$) (b), case 1c ($m = 2, p = 3$) (c) and case 1d ($m = 3, p = 5$) (d). $D = 4.4 \times 10^{-4}$ for all. The circle marks the time at which the average lithospheric stress has reduced by a factor of 2 (i.e. the decoupling timescale). The superposed patch shows the time over which stress in the neck reduces by a factor of 3 (i.e. the decoupling timescale in Bercovici et al., 2015).

dependent rheology produces slab decoupling on timescales ≤ 25 Myrs, our results support the hypothesis that rapid slab detachment may result from grain-damage, as proposed by Bercovici et al. (2015).

To compare with previous work, we note that Schmalholz (2011) found that necking and slab detachment would occur only for nonlinear (i.e. stress-dependent) viscosity. Andrews and Billen (2007), and Duretz

et al. (2012) also reported that slab detachment did not occur for linear viscosity. In contrast, our study produces necking and slab detachment for linear viscosity because of grainsize dependence. Our results are consistent with Schmalholz (2011) in that increasingly nonlinear rheology produces more rapid weakening and detachment. Duretz et al. (2012) showed that necking or viscous thinning of the slab is the

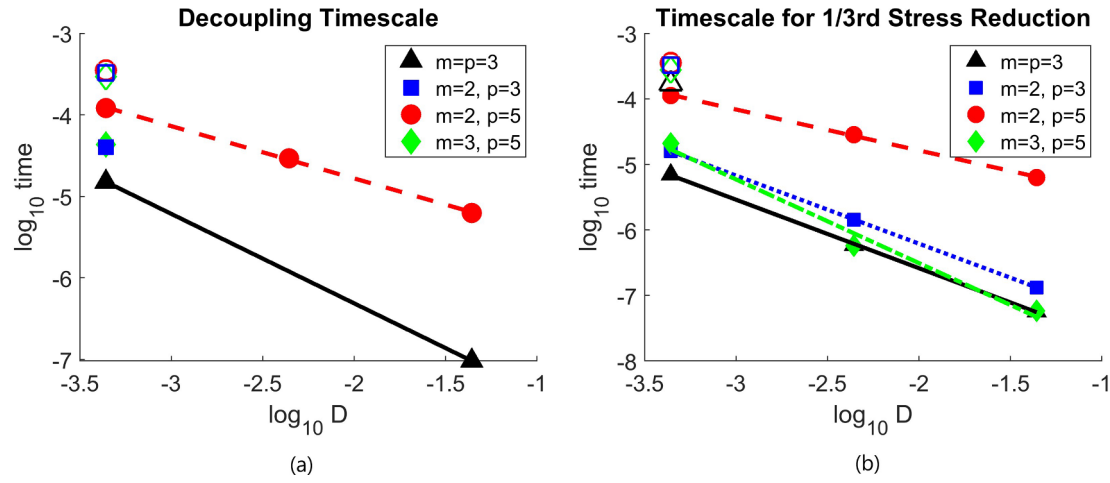


Fig. 11. The slab decoupling timescale based on reduction of lithospheric stress by a factor of 2 for linear rheology (a), and the decoupling timescales as defined in Bercovici et al., 2015 (b). Nonlinear results are plotted as open symbols. Notice that it typically takes longer for the stress to reduce by a factor of 2 in the lithosphere than by a factor of 3 in the slab (except for $m = 2, p = 5$, and nonlinear rheology models).

dominant mechanism of slab detachment and is a rapid process on geologic timescales for power law rheology (< 5 Myr). Our study considers only viscous deformation in the form of high temperature creep, and neglects brittle, semi-brittle, and low-temperature plasticity. Due to the differences in rheology, we find rapid slab detachment timescale consistent with Duretz et al. (2012) for some models, but significantly longer for others (~50 Myrs).

Our models with their simplifications and approximations also have limitations. We consider only 2D geometry in this study, while the 3D geometry of slabs may affect the detachment timescale as the necking process evolves as a lateral tear along the slab (Crameri and Tackley, 2014). The healing and damaging parameters are only marginally constrained and are expected to vary significantly. Our models only explore a subset of model parameters. Our simplified model does not account for interaction of the slab with the endothermic phase change 660 km depth in Earth's mantle, which may provide additional upward buoyancy and hinder detachment. We also do not consider the effect of water content on damage, which is expected to enhance weakening. Our models assume a simplified (e.g., vertical) slab geometry and initially uniform grainsize. Future studies need to consider more realistic situations. Finally, due to strong non-linearity in rheology, models with higher numerical resolution show more localization of weakening and more rapid damage. However, the effects are rather modest, and particularly, the overall dynamics of the necking process do not change.

5. Conclusions

In this study, we have formulated a dynamic model of slab evolution with grainsize-dependent viscosity and grainsize evolution from damage using a particle method. We have explored the characteristics of convection and the evolution of viscosity in a subducted slab using 18 model formulations (Table 2). Our findings can be summarized as follows:

- 1) Grain damage can occur with no apparent bound on how small grainsize can get for rheology with equal exponents ($m = p = 3$). This leads to very rapid weakening and the largest contrasts in grain fineness and viscosity. The grainsize is limited, however, by an

Appendix A . Non-dimensionalization of the governing equations

We begin by presenting all governing and rheological equations in dimensional form, followed by their nondimensionalization. The governing equations are given by conservation of mass, momentum, and energy in the Boussinesq approximation and infinite Prandtl number limit

$$\nabla \cdot \mathbf{u} = 0 \quad (\text{A1})$$

$$-\nabla P + \nabla \cdot [\eta(\nabla \mathbf{u} + \nabla^T \mathbf{u})] + \rho g \hat{\mathbf{e}}_z \quad (\text{A2})$$

$$\frac{\partial T}{\partial t} + \mathbf{u} \cdot \nabla T = \frac{k}{\rho c_p} \nabla^2 T, \quad (\text{A3})$$

where \mathbf{u} is the velocity vector, P the pressure, η the viscosity, ρ the density, g the acceleration due to gravity, $\hat{\mathbf{e}}_z$ the unit vector in the vertical direction, T the temperature, k the thermal conductivity, and c_p the heat capacity.

Depending on deformation mechanism (i.e. diffusion and dislocation creep), the viscosity and strain rate may take different forms. When both diffusion and dislocation creep mechanisms are present, a composite rheological formulation can be developed. The total strain rate is given by

$$\dot{\epsilon} = e^{-\frac{E}{RT}} (\eta_i \sigma^n + \eta_f \sigma A^m) \quad (\text{A4})$$

where η_i and η_f are the pre-factors associated with dislocation creep and diffusion creep, respectively, A is the fineness or inverse grainsize (Bercovici and Ricard, 2005), the exponent m is set to either 2 or 3 depending on the mode of diffusion creep, E the viscous activation energy, R the universal gas constant, σ the square-root of the 2nd invariant of the stress tensor, and exponent n for dislocation creep is 3.5. Diffusion of grains along the grain boundary (Coble creep) corresponds to $m = 3$, and diffusion through a grain (Nabarro-Herring creep) corresponds to $m = 2$. The effective viscosity for the composite rheology can be derived from Eq. (A4) as, following (Podolefsky et al., 2004)

$$\eta = \frac{1}{\eta_f} A^{-m} e^{\frac{E}{RT}} \left(1 + \left(\frac{\sigma}{\sigma_T} \right)^{n-1} \right)^{-1} \quad (\text{A5})$$

where σ_T is the transition stress. In the composite regime, the relative contribution from each of the two creep mechanisms is governed by the stress

field and the transition stress. In Newtonian models, the deformation mechanism is purely diffusion creep, so $\eta_l = 0$ in (A4), and viscosity in (A5) is reduced to

$$\frac{\eta}{\eta_f} = \frac{1}{A} A^{-m} e^{\frac{E}{RT}} \quad (A6)$$

We use a larger viscous activation energy in non-Newtonian models compared to Newtonian (Table 1).

We define the transition stress σ_T as the stress at which strain rates from diffusion and dislocation creep are equal (Hirth and Kohlstedt, 2003; Podolefsky et al., 2004)

$$\eta_f \sigma_T e^{-\frac{E}{RT} A^m} = \eta_l \sigma_T^n e^{-\frac{E}{RT}} \quad (A7)$$

solving for transition stress

$$\sigma_T = \left(\frac{\eta_f}{\eta_l} A^m \right)^{\frac{1}{n-1}} \quad (A8)$$

Note that σ_T depends on grainsize. Where the stress is larger than the transition stress, dislocation creep is the dominant deformation mechanism, and fineness-dependence of viscosity reduces with increasing stress. Where the stress is less than the transition stress, diffusion creep is the dominant deformation mechanism, and stress dependence of viscosity reduces with reducing stress. Note this only applies for non-Newtonian rheology.

Viscosity evolves with changing grainsize, temperature, and stress. The evolution of fineness, equated to the inverse grainsize, is governed by

$$\frac{dA}{dt} = \frac{f}{\gamma} \Psi - h A^p \quad (A9)$$

following (Landuyt et al., 2008) where h is the healing parameter given by

$$h = h_0 e^{-\frac{E_h}{RT}}, \quad (A10)$$

and f is the damage partitioning function which can vary from zero to one, γ the free surface energy, Ψ the deformational work, the exponent p is set to either 3 or 5, E_h the grain growth activation energy, and h_0 the healing pre-factor. When p is set to 3, the model grain assemblage is monomineralic, whereas when $p = 5$, the model grain assemblage is polymimetic (Bercovici and Ricard, 2012).

To nondimensionalize the governing equations we define nondimensional parameters $\Theta = \frac{T - T_s}{\Delta T}$, where $\Delta T = T_m - T_s$ is the temperature difference across the mantle, $\eta_r \eta' = \eta$, $\frac{\eta_r}{t_r} P' = P$, and $t_r t' = t$, where $t_r = \frac{d^2}{\kappa}$ and η_r is the reference viscosity that is chosen to be the far-field background viscosity (i.e., 10^{21} Pa s in Table 2). The dimensionless equations of mass, momentum and energy conservation follow from simply introducing these parameters, and are given by Eqs. (1)–(3) in the main text, in which Ra is the Rayleigh number that governs the vigor of convection, given by

$$Ra = \frac{\rho g \alpha \Delta T d^3}{\kappa \eta_r} \quad (A11)$$

To nondimensionalize viscosity Eq. (A5), we define $\eta = \eta_r \eta'$, $\Theta_s = \frac{T_s}{\Delta T}$, $E = R \Delta T E'$, with reference temperature $T = T_m$ or equivalently $\Theta = 1$, reference fineness $A = A_r A'$, stress $\sigma = \sigma_0 \sigma'$, and transition stress $\sigma_T = \sigma_0 \sigma_T'$, and the reference viscosity η_r is given as

$$\eta_r = \eta_f A_r^{-m} e^{\frac{E}{RT_m}} \left(1 + \left(\frac{\sigma_r}{\sigma_{Tr}} \right)^{n-1} \right)^{-1}, \quad (A12)$$

where σ_r and σ_{Tr} are reference far-field mantle stress and transition stress. In this study, σ_r is chosen to be 0.44 MPa for all non-Newtonian models (to be consistent with the average of the rescaled far-field background stress), and we choose σ_{Tr} from 1 MPa to 10 MPa which is significantly larger than σ_r . The dimensionless viscosity follows simply and is given by Eqs. (4) and (5) in the main text. Dimensionless viscosity far away from the slab is always close to 1 (Fig. 1c and e). The only constraint we impose is the reference viscosity, $\eta_r = 10^{21}$ Pa s, and it is evident from Eq. (A12) that we cannot uniquely determine the reference fineness A_r due to trade-off with η_f and other parameters.

To non-dimensionalize the fineness evolution equation, we define $\frac{\eta_r}{t_r^2} \Psi' = \Psi$, and $h_m h' = h$ with reference healing parameter h_m defined at $\Theta = 1$ (i.e. dimensionless ambient mantle temperature), to give Eqs. (6) and (7) in the main text, where D and H are dimensionless damaging and healing parameters

$$D = \frac{f \eta_r}{\gamma t_r A_r} \quad (A13)$$

$$H = t_r h_m A_r^{p-1} \quad (A14)$$

The values of D and H are determined by scaling factors which we reference from the literature (i.e. Hirth and Kohlstedt, 2003): $\eta_r = 10^{21}$ Pa s, $f = 10^{-1}-10^{-6}$, $\gamma = 1$, $t_r = 71.3$ Gyr, $A_r = 100 \text{ m}^{-1}$, and $h_m = 10^{-19}$. Damage parameter D is varied from 4.4×10^{-4} to 4.4×10^{-2} , and healing parameter H is held at a constant value of 2.3×10^5 for all models. For the sake of simplicity, we do not explore the effects of temperature- or fineness-dependence of the damage partitioning coefficient, f .

Appendix B. Solution methods

Here, we discuss in detail the subtleties of evaluating the deformational work in convection calculations. The grid-specific quantities (e.g., temperature, strain rate, and stress) that enter the fineness evolution equation (i.e., Eq. (6)) are interpolated onto the particles to update the fineness field. The interpolation of temperature is straightforward and is done using the linear shape functions of the finite elements. However, the fact that different particles can have different fineness values means that there are sub-grid scale viscosity variations in our model. To what degree the sub-

grid scale variations should be included in the evaluation of deformational work is a matter which requires some scrutiny.

The grid-scale viscosity and the strain rate obtained from solving the momentum equation can be used to estimate the grid-scale stress field, according to the constitutive relation (Eq. (A4)). When projecting the strain rate (or stress) field from the grid onto the particles, the question arises as to whether particles with different viscosities (due to the fineness variation) will experience different stress (or accommodate a different amount of strain rate). This will determine the variation in the deformational work on the particle scale.

On the one hand, we can project the grid-scale variations in stress, strain rate, viscosity, and hence deformational work onto the sub-grid scale. This corresponds to computing all quantities on the grid (i.e. solving the momentum equation) and projecting onto particle locations using linear shape functions. The work will thus vary from one particle to next, but it will do so smoothly, as dictated by the element-wise continuous shape functions. Note that this is the approach we use in the advection scheme when updating the positions of the particles.

On the other hand, we can allow for sub-grid scale variations in viscosity to dictate the deformational work. Assuming the particles see the stress interpolated from the grid but accommodate the strain rate as dictated by their individual viscosities, is analogous to assuming that damage is dictated by the weakest part of the material. Alternatively, if the strain rate is interpolated from the grid onto the particles, but the stress varies according to the particle viscosity, then this is analogous to assuming that the damage is dictated by the strongest part of the material. Thus, the evolution of viscosity will depend on whether we use the grid values of stress or strain rate for computing the deformational work rate at the particle scale.

We run some test cases to illustrate how the different assumptions about the bulk materials properties are manifested in the solution. When the stress is interpolated from the grid, damage is more extensive and more rapid compared to the linear-projection approach. When the strain rate is interpolated from the grid, damage occurs at a slower rate and overall to lesser extent compared to the linear-projection approach. Since sub-grid scale variations in viscosity, strain rate, and stress fields are not resolved on the finite element grid, it is most consistent with the continuum assumptions (i.e., a continuously smooth medium) to only use grid-scale variations in the work term. In the same regard, it is not consistent with the continuum approximation to use the individual particles viscosity when evaluating deformational work.

Appendix C. Supplementary data

Supplementary data to this article can be found online at <https://doi.org/10.1016/j.pepi.2018.09.001>.

References

- Andrews, E.R., Billen, M.I., 2007. Rheologic controls on the dynamics of slab detachment. *Tectonophysics* 464, 60–69.
- Astermann, J., et al., 2011. Quantifying the forces needed for the rapid change of pacific plate motion at 6 Ma. *Earth Planet. Sci. Lett.* 307, 289–297.
- Bercovici, D., Ricard, Y., 2005. Tectonic plate generation and two-phase damage: void growth versus grainsize reduction. *J. Geophys. Res.* 110, B03401. <https://doi.org/10.1029/2004JB003181>.
- Bercovici, D., Ricard, Y., 2012. Mechanisms for the generation of plate tectonics by two-phase grain-damage and pinning. *Phys. Earth Planet. Int.* 2755, 202–203.
- Bercovici, D., Ricard, Y., 2013. Generation of plate tectonics with two phase grain-damage and pinning: source-sink model and toroidal flow. *Earth Planet. Sci. Lett.* 365, 275–288.
- Bercovici, D., Ricard, Y., 2014. Plate tectonics, damage and inheritance. *Nature* 508, 513–516.
- Bercovici, D., Ricard, Y., 2016. Grain-damage hysteresis and plate-tectonic states. *Phys. Earth Planet. Int.* 253, 31–47. <https://doi.org/10.1016/j.pepi.2016.01.005>.
- Bercovici, D., Skemer, P., 2017. Grain damage, phase mixing and plate-boundary formation. *J. Geodyn.* 108, 40–55. <https://doi.org/10.1016/j.jog.2017.05.002>.
- Bercovici, D., Schubert, G., Ricard, Y., 2015. Abrupt tectonics and rapid slab detachment with grain-damage. *Proc. National Acad. Sci.* 112.5, 1287–1291 to appear.
- Billen, M.I., 2008. Modeling the dynamics of subducting slabs. *Annu. Rev. Earth Planet. Sci.* 36, 325–356.
- Crameri, F., Tackley, P.J., 2014. Spontaneous development of arcuate single-sided subduction in global 3-D mantle convection models with a free surface. *J. Geophys. Res. Solid Earth* 119 (7), 5921–5942. <https://doi.org/10.1002/2014JB010939>.
- Duretz, T., Schmalholz, S., Gerya, T., 2012. Dynamics of slab detachment. *Geochem. Geophys. Geosyst.* 13, 1525–2017. <https://doi.org/10.1029/2011GC004024>.
- Foley, B.J., Bercovici, D., 2014. Scaling laws for convection with temperature-dependent viscosity and grain-damage. *Geophys. J. Int.* 199, 580–603. <https://doi.org/10.1093/gji/ggu275>.
- Foley, B.J., Bercovici, D., Landuyt, W., 2012. The conditions for plate tectonics on super-earths: inferences from convection models with damage. *Earth Planet. Sci. Lett.* 331–332 (281), 290.
- Fukao, Y., Widjiantor, S., Obayashi, M., 2001. Stagnant slabs in the upper and lower mantle transition region. *Rev. Geophys.* 39, 291–323.
- Gerya, T.V., Yuen, D.A., Maresch, W.V., 2004. Thermomechanical modeling of slab detachment. *Earth Planet. Sci. Lett.* 226, 101–116.
- Hager, O'Connell, 1981. A simple model of plate dynamics and mantle convection. *J. Geophys. Res.* 84, 4843–4867.
- Hillebrand, B., Thieulot, C., Geenen, T., van den Berg, A.P., Spakman, W., 2014. Using the level set method in geodynamical modeling of multi-material flows and Earth's free surface. *Solid Earth* 5, 1087–1098.
- Hirth, G., Kohlstedt, D., 2003. Rheology of the Upper Mantle and the Mantle Wedge: A View from the Experimentalists. *American Geophys. Union Inside the Subduction Factory*, pp. 83–105.
- Landuyt, W., Bercovici, D., Ricard, Y., 2008. Plate generation and two-phase damage theory in a model of mantle convection. *Geophys. J. Int.* 174 (3), 1065–1080.
- McNamara, A.K., Zhong, S.J., 2004. The influence of thermochemical convection on the fixity of mantle plumes. *Earth Planet. Sci. Lett.* 222, 485–500.
- Montési, L., Hirth, G., 2003. Grain size evolution and the rheology of ductile shear zones: from laboratory experiments to post-seismic creep. *Earth Planet Sci. Lett.* 211, 97–110.
- Moresi, L.N., Solomatov, V.S., 1995. Numerical investigation of 2d convection with extremely large viscosity variations. *Phys. Fluids* 7, 2154–2162.
- Mulyukova, E., Bercovici, D., 2017b. Formation of lithospheric shear zones: effect of temperature on two-phase grain damage. *Phys. Earth. Planet. Int.* 270, 195–212.
- Mulyukova, E., Bercovici, D., 2017a. Collapse of passive margins by lithospheric damage and plunging grain size. *Earth and Planetary Science Letters* (submitted).
- Podolefsky, N., Zhong, S.J., McNamara, A., 2004. The anisotropic and rheological structure of the oceanic upper mantle from a simple model of plate shear. *Geophys. J. Int.* 158, 287–296.
- Ricard, Y., Bercovici, D., 2009. A continuum theory of grain size evolution and damage. *J. Geophys. Res.* 114, B01204. <https://doi.org/10.1029/2007JB005491>.
- Richards, M., Lithgow-Bertelloni, C., 1996. Plate motion changes, the Hawaiian-emperor bend, and the apparent success and failure of geodynamical models. *Earth Planet. Sci. Lett.* 137, 1927.
- Schmalholz, S., 2011. A simple analytical solution for slab detachment. *Earth Planet. Sci. Lett.* 304, 45–54.
- Schubert, G., Turcotte, D., Olson, P., 2001. *Mantle Convection in the Earth and Planets*. Cambridge Univ Press.
- Stegman, D.R., Schellart, W.P., Freeman, J., 2010. Competing influences of plate width and far-field boundary conditions on trench migration and morphology of subducted slabs in the upper mantle. *Tectonophysics* 483, 46–57.
- Tackley, P.J., King, S.D., 2003. Testing the tracer ratio method for modeling active compositional fields in mantle convection simulations. *Geochem. Geophys. Geosyst.* 4, 1525–2027.
- van Hunen, J., Zhong, S.J., Shapiro, N.M., Ritzwoller, M.H., 2005. New evidence for dislocation creep from 3-D geodynamic modeling the Pacific upper mantle structure. *Earth Planet. Sci. Lett.* 238, 146–155.
- von Blanckenburg, F., Davies, J., 1995. Slab breakoff – a model for syncollisional magmatism and tectonics in the alps. *Tectonics* 14, 120–131.
- Wortel, M., Spakman, W., 2000. Geophysics – subduction and slab detachment in the Mediterranean-Carpathian region. *Science* 290, 1910–1917.
- Zhong, S.J., McNamara, A.K., Tan, E., Moresi, L., Gurnis, M., 2008. A benchmark study on mantle convection in a 3-D spherical shell using CitcomS. G'3 <https://doi.org/10.1029/2008GC002048>. Q10017.